

MATERIALS SCIENCE

Intrinsically stretchable organic light-emitting diodes

Jin-Hoon Kim and Jin-Woo Park*

Soft and conformable optoelectronic devices for wearable and implantable electronics require mechanical stretchability. However, very few researches have been done for intrinsically stretchable light-emitting diodes. Here, we present an intrinsically stretchable organic light-emitting diode, whose constituent materials are all highly stretchable. The resulting intrinsically stretchable organic light-emitting diode can emit light when exposed to strains as large as 80%. The turn-on voltage is as low as 8 V, and the maximum luminance, which is a summation of the luminance values from both the anode and cathode sides, is 4400 cd m⁻². It can also survive repeated stretching cycles up to 200 times, and small stretching to 50% is shown to substantially enhance its light-emitting efficiency.

INTRODUCTION

Soft electronics that flex and stretch have been rapidly developed and show potential for notably affecting our daily lives (1–3). A stretchable organic light-emitting diode (OLED) is one of the key components of stretchable displays, enabling expandable and foldable smartphones, rollable or collapsible wallpaper-like televisions, and neurological or epidermal medical devices (1, 3, 4). All of the materials and components of such OLEDs need to be stretchable and mechanically robust (5–7). The current technology for stretchable OLED display panels combines elastic interconnects with rigid LEDs (5, 8, 9). As an alternative, an intrinsically stretchable (*is*-) OLEDs in which all constituent materials are inherently stretchable will enable higher mechanical deformability and robustness, higher device density, and improved skin or tissue compatibility (10, 11). Various strategies have been suggested for designing stretchable conjugated polymeric materials for *is*-transistors (5, 6, 12). However, the production of *is*-OLEDs is still largely in its infancy (1, 13, 14).

The first *is*-organic light-emitting device, and perhaps the first *is*-organic electronic device of any kind, was an organic light-emitting electrochemical (LEC) device reported in 2011 (14). The electrodes were based on carbon nanotubes, and the blue emissive polymer used was PF-B, a polyfluorene copolymer (14). This structure has long alkyl side chains, consistent with the level of possible deformability, and was mixed with the ionic conductor poly(ethylene oxide) dimethacrylate ether and lithium trifluoromethane sulfonate (14). The authors later showed a yellow emissive device using the poly(phenylenevinylene) (PPV) derivative, “Super Yellow (SY),” which achieved an impressive extensibility of 120% (1, 13). However, the authors did not investigate the mechanical properties and the stretchability mechanism of the constituent materials for *is*-OLEDs. Since then, little has followed the previous work.

RESULTS

To develop *is*-OLEDs with superior mechanical stretchability, the unique *is*-constituent materials were designed in this work. First, for the *is*-emissive material layer (*is*-EML), a small-molecule non-ionic surfactant (Triton X) was mixed as a plasticizer with a commercial emissive material (SY). The chemical structures of SY and Triton X are shown in Fig. 1A. The plasticizer can increase the free

volume of the conjugated polymer by reducing the interchain interactions (15), thus making SY become softer and more stretchable.

To verify our strategy, the mechanical properties [Young’s modulus, crack density, and crack onset strain (COS)] of pristine SY and *is*-EMLs (ST1 to ST4 in Fig. 1A) were investigated, with the results shown in Fig. 1B, figs. S1 and S2, and table S1. As expected, *is*-EML with a small amount of Triton X (ST1 in Fig. 1A) exhibits a 25% lower Young’s modulus than that of pristine SY. As the weight ratio of Triton X increases, the Young’s modulus further decreases to 15 MPa, as shown in Fig. 1B. In addition, the crack density and COS in *is*-EML were substantially reduced and improved, respectively, with the increase of the Triton X weight content as compared with that of pristine SY (Fig. 1B and fig. S2C). The change in Young’s modulus, crack density, and COS verified that Triton X can effectively modulate the mechanical properties of the light-emitting conjugated polymers.

The major challenge faced in developing *is*-EML lies in simultaneously maintaining good electrical and mechanical properties (6). As Triton X is an electrical insulator, its effect on the electrical properties of *is*-EMLs was also investigated. The carrier mobilities (hole mobility, μ_h , and electron mobility, μ_e) of *is*-EMLs were analyzed by fabricating hole- and electron-only devices (16). The detailed device structure and current density (J)–voltage (V) curves are shown in figs. S3 and S4, respectively. As shown in Fig. 1C, μ_h and μ_e values of pristine SY are approximately 9×10^{-7} and 3×10^{-7} cm⁻² V⁻¹ s⁻¹, respectively (17, 18). Both μ_h and μ_e were notably decreased as the weight of Triton X added to SY increases to 1:1 (ST3) and 1:2 (ST4) due to the electrically insulating nature of Triton X. However, when the weight ratio of SY to Triton X is 5:1 (ST1) and 2:1 (ST2), both μ_h and μ_e become slightly higher than that of pristine SY, which confirms that, at the optimized weight ratio, Triton X improves the electrical properties of *is*-EML by changing the conformation of the SY chains. On the basis of the electrical and mechanical analysis in Fig. 1 (B and C), ST2 was chosen as *is*-EML for *is*-OLED.

To explain how Triton X affects the conformation and microstructure of SY chains, dynamic mechanical analysis (DMA) was performed to analyze the glass transition temperature (T_g) of pristine SY and ST2 to ST4 (19). When a small-molecule plasticizer is blended in polymer matrices, it reduces the interchain interaction of the polymer chains (20). Hence, the chain mobility and free volume of the polymer chains are increased, thus decreasing T_g of the polymer matrices (12). According to Fig. 1D and fig. S5, T_g of pristine SY is 82.1°C (21). However, T_g of ST2 is substantially reduced to

Copyright © 2021
The Authors, some
rights reserved;
exclusive licensee
American Association
for the Advancement
of Science. No claim to
original U.S. Government
Works. Distributed
under a Creative
Commons Attribution
NonCommercial
License 4.0 (CC BY-NC).

Downloaded from <http://advances.sciencemag.org/> on February 24, 2021

Department of Materials Science and Engineering, Yonsei University, Seoul 03722, Korea.
*Corresponding author Email: jwpark09@yonsei.ac.kr

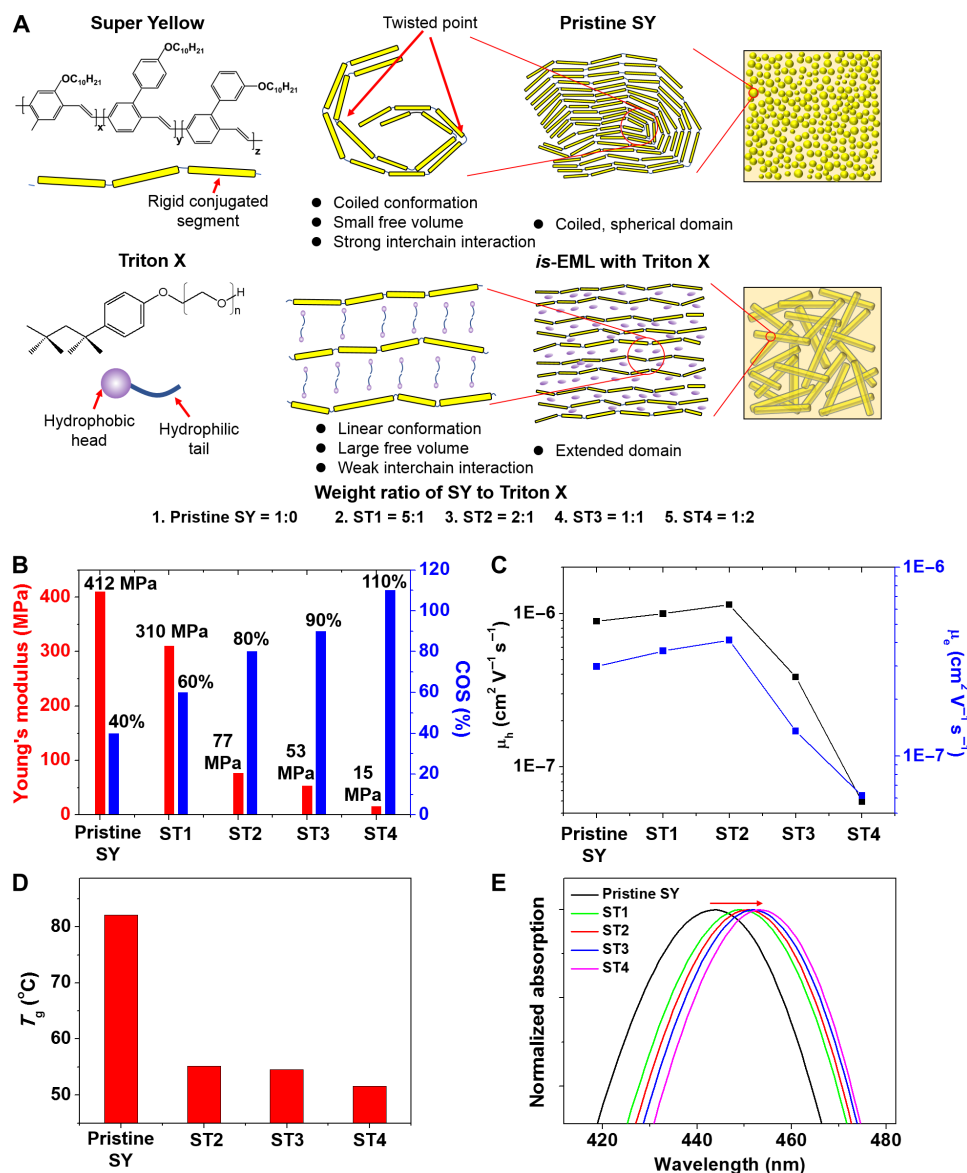


Fig. 1. Design of *is*-OLEDs and characterization of *is*-EML. (A) Schematics comparing the microstructures of pristine SY and *is*-EMLs designed in this study. (B) Mechanical properties of pristine SY and *is*-EML thin films. (C) Carrier mobility of pristine SY and *is*-EMLs measured through the hole- and electron-only devices. (D) T_g of pristine SY and *is*-EMLs measured by DMA. (E) UV-vis absorption spectra of pristine SY and *is*-EMLs. On the basis of the various analysis results, by adding Triton X into SY, the SY chains become extended. Hence, a fibrillar microstructure with elongated domains is formed, which is favorable for stretchable electronics.

55.2 $^{\circ}\text{C}$, and increasing the weight ratio of Triton X, T_g further decreases to 51.6 $^{\circ}\text{C}$. Hence, Triton X addition reduced the interchain interaction between the SY chains, thereby making SY softer and more stretchable. However, such results contrast with the carrier mobility analysis shown in Fig. 1C. The charge carrier mobilities of the conjugated polymers tend to decrease due to reduced interchain charge carrier transport (22). Hence, there should be another mechanism underlying the carrier mobility increase in *is*-EMLs.

The chain conformation of pristine SY and *is*-EMLs was also analyzed by ultraviolet-visible (UV-vis) absorption (23–25). According to the UV-vis absorption spectra in Fig. 1E, the peak wavelength of *is*-EMLs is slightly redshifted with increasing Triton X, which indicates that the conjugation length of the SY chains of *is*-EMLs is extended (24–26). On the basis of this, we can presume that the conformation

of the SY chain is changed from a coiled to a linear structure. To further verify the chain conformation change, Raman spectroscopy was performed. According to the detailed Raman spectra shown in fig. S6B, the main peaks are observed at 1112, 1270, 1310, 1585, and 1625 cm^{-1} , which are similar to those of poly[2-methoxy-5-(2-ethylhexyloxy)-1,4-phenylenevinylene] (24, 27).

As shown in fig. S6C and table S2, the intensity ratio of 1580 to 1625 cm^{-1} (I_{1580}/I_{1625}) tends to increase with Triton X, which also strongly confirms that the conjugation length of the SY chain increases with the addition of Triton X (23, 27). This explains the high carrier mobility of ST2 in Fig. 1C. In polymer chains with a coiled conformation, electron delocalization is hindered at the twisted point (25). Hence, the carrier mobility of the conjugated polymers tends to increase as the conjugation length increases via polymer chain extension (26, 28).

On the basis of our DMA, UV-vis absorption, and Raman spectroscopy results, the microstructure of *is*-EMLs and pristine SY from the molecular scale to the macroscale can be presumed to be as schematically shown in Fig. 1A. The SY chains in *is*-EMLs are extended at the molecular level due to the decreased interchain interaction arising from the plasticizing effect of Triton X. As a result, an extended domain is formed, as shown in Fig. 1A, which results in a fibrous structure with increased stretchability. The presumed microstructures described in Fig. 1A were further verified by atomic force microscopy (AFM). As shown in fig. S7, the microstructure of *is*-EMLs is changed from spherical domains to a fibrous structure, which strongly supports our assumption of a conformational change of the SY chains in *is*-EMLs. Although the surface roughness (R_q) of *is*-EMLs slightly increased as the amount of Triton X increased, R_q of *is*-EMLs was still lower than 1 nm, which is suitable for the *is*-OLED device fabrication. Such conformation change of the SY chains by the addition of Triton X also explained the electrical mobility increase in ST1 and ST2 because the increase of the intrachain

conjugation also increases the carrier mobility of the conjugated polymers through enhancement in the intrachain carrier transport (29).

To obtain an *is*-hole transport layer (*is*-HTL), Triton X was added to poly(3,4-ethylenedioxythiophene):polystyrene sulfonate (PEDOT:PSS; Clevious AI 4083, Heraeus). There are two types of PEDOT:PSS: highly conductive PEDOT:PSS (commonly PH1000, Heraeus), which is used mostly for electrodes in transistors (30–32), and highly resistive PEDOT:PSS, which is used for HTL in optoelectronic devices (1, 33–35). The difference between the two types of PEDOT:PSS lies in the weight ratio between PEDOT and PSS. To date, several studies conducted to improve the stretchability of PEDOT:PSS were limited to the modification of highly conductive PEDOT:PSS (31, 32).

When added to AI 4083, Triton X can prevent strong electrostatic interactions between PEDOT and PSS, inducing phase separation in PEDOT:PSS films (30). Hence, a nanofibrous PEDOT-rich domain is formed as in the highly conductive PEDOT:PSS films during the film formation process, as shown in Fig. 2A, which is favorable for mechanical stretchability (30, 31). The weight percent of Triton X

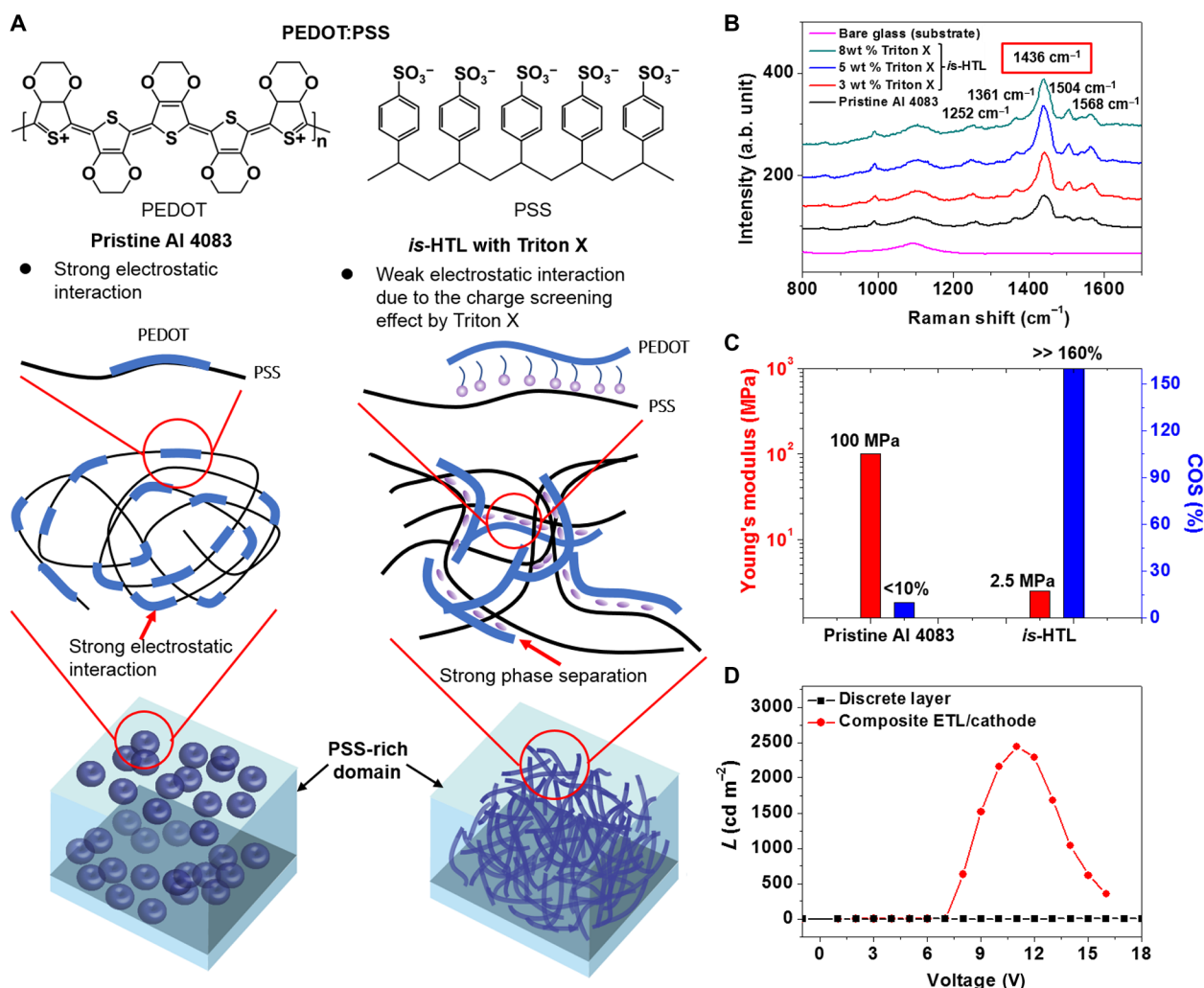


Fig. 2. Design of other *is*-functional layers and characterization. (A) Schematics of the microstructures of pristine HTL and *is*-HTL designed in this study. (B) Raman spectra of pristine AI 4083, *is*-HTL with various wt % of Triton X, and a glass substrate. (C) Mechanical properties of pristine HTL and *is*-HTL thin films. The conformation of the PEDOT chains is changed from coiled to linear with the addition of Triton X, which results in improved electrical and mechanical properties of *is*-HTL. (D) Luminescence (L)- V plot of OLEDs with the solution-processed *is*-ETL and *is*-cathode with a discrete layer and a composite-like structure.

was optimized on the basis of the hole transport property of *is*-HTL evaluated through the use of HTL-only devices [indium tin oxide (ITO)/*is*-HTL/Au] and OLEDs with conventional structures (fig. S8). As shown in fig. S8A, when *is*-HTL with 5 weight % (wt %) Triton X was used, ITO/*is*-HTL/Au devices showed the highest *J* value, and OLEDs showed performances comparable to those of OLEDs with pristine AI 4083, as shown in fig. S8B.

The change in the charge transport property of *is*-HTL with the addition of Triton X was analyzed using Raman spectroscopy. As shown in Fig. 2B, the Raman peak centered at 1436 cm^{-1} of *is*-HTL is broader and more intense than that of pristine AI 4083. Furthermore, the intensity of 1436 cm^{-1} peak was the highest when 5 wt % of Triton X was added to AI 4083. In PEDOT:PSS, the peak centered at 1436 cm^{-1} is assigned to the $C_{\alpha} = C_{\beta}$ symmetric stretching vibration (33). The intensity increase at 1436 cm^{-1} indicates that the conformation of the PEDOT chains is changed from a benzoid (coiled) to a quinoid (linear) structure (33, 36). Hence, the Raman spectroscopy results correspond well to the hole transport property measured in fig. S8.

The mechanical properties of pristine AI 4083 and *is*-HTL were analyzed using the mechanical buckling method (12) and COS analysis. As shown in Fig. 2C, the Young's modulus of *is*-HTL with 5 wt % Triton X is substantially reduced from 100 to 2.5 MPa. In addition, on the basis of the COS measurements, pristine AI 4083 shows severe cracks even at strains below 10% (fig. S9A). However, *is*-HTL does not show any cracks even when stretched up to 160%. This mechanical property change is due to the conformational change of the PEDOT:PSS films after the addition of Triton X (31, 32).

To further verify the change in the conformation of *is*-HTL, x-ray photoelectron spectroscopy (XPS) and AFM analyses were performed. According to the XPS surface analysis results in fig. S9C, the intensity ratio between the S_{2p} bands from PEDOT and PSS increases with the addition of Triton X, which also supports the conformational change of the PEDOT chains in *is*-HTL (33). The conformational change of the PEDOT chains was also verified by microstructural analysis by AFM. As shown in fig. S9D, the PEDOT-rich domain is changed from a spherical to a fibrous structure (31, 32). The linear conformation is more favorable for efficient charge transport.

For *is*-ETL, doped polyethyleneimine ethoxylated (d-PEIE) and ZnO nanoparticles were used together. In previous works by others, the strong dipole layer formed by the amine moiety in PEIE could substantially reduce the work function of the cathode material, improving the electrical injection from the cathode (37). In addition, in our previous work, when a small amount of an n-type dopant (Cs_2CO_3 in this work) was added to PEIE, the work function of the cathode was further decreased (38). Moreover, PEIE was expected to be mechanically stretchable due to its low T_g of -25°C and strong hydrogen bonding arising from the amine functional moiety (39, 40). Among various nanoparticles, ZnO nanoparticles were selected because of their superior electron injection properties (41). According to the field emission scanning electron microscopy (FE-SEM) analysis in fig. S10A, *is*-ETL does not show any cracks during and after stretching to 100%.

For *is*-cathode and *is*-anode, one-dimensional silver nanowire (AgNW) networks were used. *is*-ETL was coated on AgNWs to form a composite structure. OLEDs with such a composite structure of *is*-ETL/AgNWs show very stable operation and good performance with an L_{max} of 2500 cd m^{-2} , as shown in Fig. 2D and fig. S10B. The

significant improvement in the OLEDs' performance was due to the efficient electron injection of the composite *is*-ETL/AgNWs/*is*-ETL structure. When AgNWs were coated on *is*-ETL, the interfacial contact area between AgNW and *is*-ETL was very small, as shown in fig. S10B. Such poor interfacial contact resulted in the inefficient electron injection from the cathode, as schematically shown in fig. S10C. Hence, OLEDs based on this type of cathode did not operate at all, as shown in Fig. 2D. To overcome this limitation, another *is*-ETL was coated again on the AgNW cathode to form the composite structure. As shown in fig. S10B, AgNWs were fully embedded in *is*-ETL. In this composite structure, the interfacial contact area between AgNWs and *is*-ETL notably improved, which enhanced electron injection behavior, as schematically shown in fig. S10C.

Static and cyclic stretching test results for the composite-type cathode are shown in fig. S11 (B and C). These results indicate that the composite structured cathode could maintain good electrical conductivity even stretched up to 100% strain and repeatedly stretched for hundreds of cycles. Furthermore, the composite structured cathode did not show any cracks on the surface after static and cyclic stretching tests (fig. S11D). Such stretching tests and surface analysis verified the good stretchability of composite structured cathode.

For *is*-anode and substrate, AgNWs and a silica aerogel composite were co-embedded in elastomeric polydimethylsiloxane (PDMS) (42). We have shown in our previous work that silica aerogels substantially improve the stretchability of AgNWs by enhancing the adhesion between AgNWs and PDMS matrices (42).

Last, *is*-OLEDs composed of *is*-anode, *is*-HTL, *is*-EML, *is*-ETL, and *is*-cathode were fabricated. Schematic descriptions of the structures and fabrication process for *is*-OLEDs are shown in Fig. 3A and fig. S12, respectively. Before fabricating the devices, the effects of solvents (isopropyl alcohol, 2-methoxyethanol, and toluene) used in this study on the thin films were analyzed first. As shown in fig. S13, SY did not show any change in its surface morphology and UV-vis absorption spectrum after the spin coating of either pure isopropyl alcohol or 2-methoxyethanol used as the solvents in the coating of *is*-ETL and *is*-cathode. Hence, there was no damage or conformational changes that occurred in SY during the consecutive solution-based coating processes.

There was a slight change in the UV-vis absorption spectrum of *is*-HTL when spin-coated with pure toluene, which was the solvent of *is*-EML (fig. S14A). Raman spectroscopy and COS analysis were performed on *is*-HTL to determine the origin of this change. As shown in fig. S14B, there was no change in Raman spectra of both pristine AI 4083 and *is*-HTL after they were spin-coated of pure toluene. Hence, the spin coating of toluene does not vary the conformation in the PEDOT chains. Furthermore, as shown in fig. S14C, *is*-HTL still showed good stretchability after the spin coating of toluene, thus verifying the absence of any conformational change in *is*-HTL. Consequently, the slight change in the UV-vis absorption spectrum of *is*-HTL in fig. S14A could be interpreted as the removal of excess Triton X from *is*-HTL. The optimized *is*-HTL had a very large amount of Triton X mixed with AI 4083 solution at 5 wt %. Although excess Triton X was removed during the spin coating of the toluene-dissolved *is*-EML, it did not seriously affect the performances of *is*-OLEDs, as it did not cause any conformation and stretchability change of the PEDOT chain in *is*-HTL.

Figure 3B shows *J-V-L* curves of *is*-OLEDs for the front (cathode) side. The *J-V-L* curves of *is*-OLEDs with different EMLs (pristine

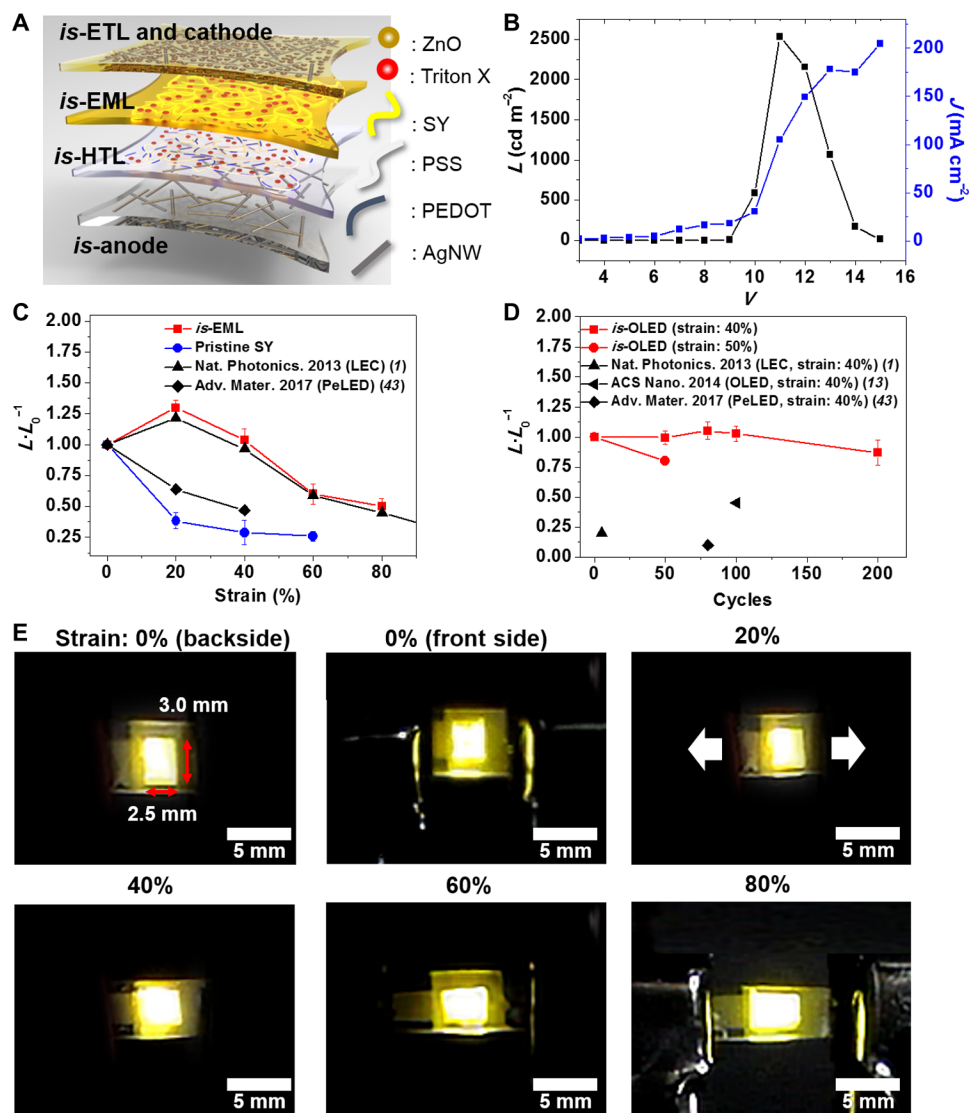


Fig. 3. Fabrication and characterization of *is*-OLEDs. (A) Schematic structure of *is*-OLEDs fabricated in this study. (B) J - V - L curve of *is*-OLEDs. (C) Relative L change (L/L_0^{-1}) of *is*-OLEDs based on pristine SY and *is*-EML during the static stretching tests. (D) L/L_0^{-1} changes of *is*-OLEDs during cyclic stretching tests. (E) Optical images of *is*-OLEDs with an original emission area of $3.0 \times 2.5 \text{ mm}^2$, operated under various strains at applied V of 9.5 V for 0, 20, and 40% strain and 9.8 V for 60 and 80% strain. All data were measured under ambient atmospheric conditions. L was measured on the basis of the emission from the cathode (front side). Photo credits (E): Jin-Hoon Kim, Yonsei University.

SY, ST1, ST3, and ST4) are shown in fig. S15. *is*-OLED using ST2 showed the highest L value, which showed a similar trend with charge carrier mobility analysis shown in Fig. 1C. As the cathode and anode are transparent, *is*-OLEDs are semitransparent (as shown in fig. S16A), emitting light from both sides. As shown in Fig. 3B, *is*-OLEDs show an L_{max} of 2500 cd m^{-2} at 11 V with a turn-on V (V_{on}) of 8.3 V for the cathode (front) side, and the L_{max} on the back (anode) side is 1900 cd m^{-2} at 11 V, as shown in fig. S16B. Such L_{max} is the highest among the values reported for *is*-LECs and *is*-OLEDs (1, 13). Moreover, in other works based on *is*-LECs and *is*-OLEDs, L_{max} was obtained at a voltage as high as 21 V (1, 13).

The stretchability of *is*-OLEDs was investigated by static and cyclic stretching tests. As shown in Fig. 3C, *is*-OLEDs based on pristine SY show poor stretchability owing to the highly brittle nature of pristine SY. However, *is*-OLEDs based on *is*-EML show superior stretchability

owing to the all-*is*-constituent materials designed in this work. As shown in Fig. 3C, the L/L_0^{-1} value of *is*-OLEDs is maintained at 1, even when OLEDs are stretched up to 40% strain, and even increases by 30% at 20% strain. Such phenomena were also observed in *is*-LECs reported by Liang *et al.* (1), which could be explained by an improvement in the interfacial charge injection and transport behavior due to the Poisson contraction during mechanical stretching. In addition, *is*-OLEDs maintain an L/L_0^{-1} of 0.5 even when stretched up to 80% strain. As shown in fig. S16C, *is*-OLEDs show an L_{max} of 1167 cd m^{-2} at 12 V and a V_{on} of 9 V even when stretched up to 80% strain. The L/L_0^{-1} values obtained from the static stretching test are the highest compared to those of other *is*-LEDs, including *is*-LECs (1) and *is*-perovskite LEDs (*is*-PeLEDs) (43) reported by others.

Such superior mechanical stretchability of *is*-OLEDs leads to a marked improvement in the cyclic stretching tests. As shown in

Fig. 3D, *is*-OLEDs show almost constant $L \cdot L_0^{-1}$ during cyclic stretching at 40% strain. Furthermore, more than 90% of the initial L of *is*-OLEDs is maintained even after 200 cycles at 40% strain. Moreover, *is*-OLEDs show an $L \cdot L_0^{-1}$ of 0.8 for 50 cycles at 50% strain. In contrast, as shown in Fig. 3D, *is*-LEDs reported by others show severe degradation even after a few stretching cycles (1, 13, 43). For *is*-LECs, *is*-PeLEDs, and *is*-OLEDs, $L \cdot L_0^{-1}$ substantially decreases to 0.2, 0.1, and 0.45 after only 5, 80, and 100 cycles of stretching at 40% strain, respectively (1, 13, 43).

The current efficiency (ϵ_c) of *is*-OLEDs based on *is*-EML and pristine SY is about 1.6 and 1.7 cd A^{-1} , respectively. Such a similar ϵ_c value is due to the increased J value in *is*-OLEDs with *is*-EML, as shown in fig. S15. As shown in fig. S16H, the ϵ_c value of *is*-OLEDs slightly increases from 1.6 to 2.0 cd A^{-1} with stretching cycles. The increase in ϵ_c of *is*-OLEDs after cyclic stretching originated from the formation of the buckling waves during the cyclic stretching. As shown in fig. S17A, several buckling wave patterns were observed on the surface of *is*-OLEDs after the cyclic stretching due to the mismatch in the Young's moduli of the *is*-OLED functional layers. These buckling wave patterns could enhance the light output by effectively extracting the trapped light in the devices (44). Optical images of *is*-OLEDs stretched up to various strains are shown in Fig. 3E. Uniform light emission is observed even up to 80% strain.

Cross-sectional transmission electron microscopy (TEM) analysis was used to analyze the structure of *is*-OLEDs and determine whether any delaminations occurred in *is*-OLEDs after mechanical stretching. Before stretching, *is*-OLEDs showed discrete interfaces between their functional layers, with each layer clearly distinguished through energy-dispersive spectroscopy (EDS) mapping shown in fig. S17B. Consequently, no observable delamination was seen in *is*-OLEDs even after being stretched up to 80% strain. Hence, all layers used in *is*-OLEDs could maintain good adhesion even during mechanical stretching.

Because the all-*is*-constituent materials used in this work were solution processable, the size of *is*-OLEDs is highly scalable. As shown in Fig. 4A, *is*-OLEDs with device areas up to $6 \times 9 \text{ mm}^2$ and $5 \times 5 \text{ mm}^2$ were successfully fabricated, and uniform emission throughout the area (cathode side) is observed with an L_{max} of 1800 cd m^{-2} at 10 V. In addition, *is*-OLEDs can be stretched up to 60% strain with an $L \cdot L_0^{-1}$ of over 0.5. Also, the biaxial stretchability could be verified by poking *is*-OLEDs with a sharp tip. As shown in Fig. 4B and movie S1, *is*-OLEDs

showed stable operation even when poked by the tip of a ballpoint pen with a tip radius of 0.7 mm. *is*-OLEDs based on red-, green-, and blue-emitting polymers were fabricated to verify the applicability of *is*-OLEDs in real displays (45). To design *is*-EMLs, Triton X was added to commercial polymers emitting three colors. The performance of *is*-OLEDs with red-, green-, and blue-emitting polymers was slightly increased with the addition of Triton X. Such trend was analogous to *is*-OLEDs based on SY. As shown in Fig. 4C, red, green, and blue *is*-OLEDs could be fabricated and stretched up to 60% strain with an $L \cdot L_0^{-1}$ of over 0.5.

DISCUSSION

In this work, we presented a framework for designing *is*-constituent materials including *is*-emitting materials for *is*-OLEDs. Through various analyses, the small molecular nonionic surfactant was verified to be capable of modifying the mechanical properties of conjugated polymers via the plasticizing effect. The electrical properties of *is*-EMLs and *is*-HTL were also confirmed to change little with the highly improved mechanical properties. *is*-OLEDs based on these *is*-constituent materials showed superior mechanical stretchability compared to previously reported *is*-LEDs. The performances of *is*-OLEDs did not change even after being stretched for 200 cycles at 40% strain. In addition, *is*-OLEDs could be fabricated in a large area and be three-dimensionally stretchable. Last, we showed that our design strategy can be extended to materials emitting in various colors. The material design and fabrication process suggested in this work can provide a new paradigm for stretchable optoelectronics including three-dimensional displays, wearable biomedical information displays, photovoltaics, photodetectors, and various other LEDs.

The stability of *is*-OLEDs should be improved for practical applications. As shown in fig. S18A, the time it takes L of *is*-OLED to drop from L_0 of 100 cd m^{-2} down to 50% of L_0 (LT_{50}) was around 27 s. Furthermore, when *is*-OLEDs were stretched up to 40 and 60% strain, LT_{50} was about 12 s. After 100 and 200 cycles of stretching at 40% strain, LT_{50} was about 24 s. The LT_{50} measurement results indicate that *is*-OLEDs were not stable during the operation. There are several reasons for the performance instability of *is*-OLEDs. Because there were no suitable stretchable encapsulation materials for *is*-OLEDs, *is*-OLEDs should undergo severe degradation due to exposure to

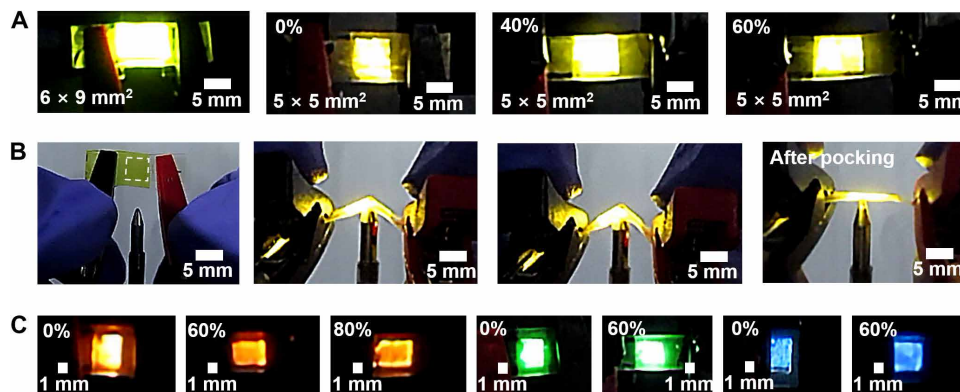


Fig. 4. Various applications of *is*-OLEDs in deformable displays. (A) Optical photographs of *is*-OLEDs with a large device area at applied V of 9.5 V. (B) Optical photographs of *is*-OLEDs being poked by a ballpoint pen with a tip radius of 0.7 mm at applied V of 9.5 V. The dashed line defines the device area. (C) Optical photographs of *is*-OLEDs based on red (at applied V of 12 V), green (at applied V of 12 V), and blue light-emitting polymers (at applied V of 8 V). The possibility of applying *is*-OLEDs to deformable displays with various form factors is shown. Photo credits (A to C): Jin-Hoon Kim, Yonsei University.

oxygen and moisture during device operation. Hence, encapsulation materials for stretchable electronics should be developed to be applied in real applications.

Another reason for the *is*-OLED performance instability was the very high operational V of *is*-OLEDs shown in Fig. 3A. Such high operating V resulted into very high operation temperature, as shown in fig. S18B, which should cause severe thermal degradation of organic layers in *is*-OLEDs. Hence, the operating V of *is*-OLEDs also needs to be lowered by further optimizing the thickness of the active layers and effective energy level alignment between *is*-constituent materials. Last, the nanoscale protrusions were observed on the surface of *is*-anode, as shown in fig. S18C. Such protrusions evolved during the release of the embedded *is*-anodes from a sacrificial layer. These protrusions could lead to a catastrophic failure during the device operation because electrical currents could concentrate on these protrusions, resulting in severe degradation of organic layers in *is*-OLEDs. Hence, these issues should be resolved to improve the stability of *is*-OLEDs.

MATERIALS AND METHODS

Preparation of *is*-EML and *is*-HTL solutions

For preparation of the *is*-EML solution, Triton X (Sigma-Aldrich) was first dissolved in toluene at a certain concentration (from 1 to 10 mg ml⁻¹). Then, SY (Sigma-Aldrich) was dissolved in the Triton X–dissolved toluene at a concentration of 5 mg ml⁻¹. For pristine SY, SY was dissolved in pure toluene at a concentration of 5 mg ml⁻¹. This solution was stirred using a magnetic stirrer at 300 rpm for 6 hours at room temperature.

For the *is*-HTL solution, various weight ratios of Triton X (from 3 to 8 wt %) were dissolved in a PEDOT:PSS solution (AI 4083, from Heraeus). Then, isopropyl alcohol was added to the *is*-HTL solution at a weight ratio of 1:1. This solution was stirred using a magnetic stirrer at 450 rpm for 1 hour at room temperature.

Mechanical characterization of *is*-EMLs and *is*-HTL

For COS analysis, PDMS film was prepared by mixing the base and a curing agent (Sylgard 184 elastomer kit from Dow Corning) at a weight ratio of 10:1. This liquid mixture was spin-coated at 500 rpm for 30 s on a polyethylene terephthalate (PET) substrate and cured at 120°C for 12 hours. Then, the cured PDMS film was peeled off from the PET substrate.

For COS analysis of *is*-HTL, *is*-HTL solution with 5 wt % Triton X was spin-coated on the PDMS film at 1000 rpm for 60 s. Then, *is*-HTL was annealed at 90°C for 10 min. For *is*-EML analysis, the *is*-EML solution was spin-coated on the *is*-HTL–coated PDMS substrate at 1500 rpm for 30 s and annealed at 90°C for 5 min.

Prepared specimens were cut into rectangular shapes of 25 × 5 mm². These specimens were loaded on a homemade stretching jig. Strain from 0 to 120% for *is*-EML and from 0 to 160% for *is*-HTL was applied, and crack formation was observed at every 10% strain using optical microscopy (OM). For the crack density analysis of *is*-EML, the number of cracks was counted while the strain was maintained at 100%.

For Young's modulus analysis, the mechanical buckling method was used. First, a self-assembled monolayer (SAM) was formed on a glass substrate using a silane solution (Sigma-Aldrich). For the SAM treatment, a glass substrate was placed in a vacuum chamber, and the silane solution was dropped near the glass substrate. Then, vacuum pumping was performed for 30 min, followed by thermal

annealing at 130°C for 30 min. Pristine SY and *is*-EML were coated on this SAM-treated glass at 1500 rpm for 30 s and thermally annealed at 90°C for 5 min. Then, prestretched PDMS was conformally attached on the films. Last, PDMS was detached from the glass substrate, and the prestrain was released. During this process, pristine SY and *is*-EML were transferred to PDMS, and mechanical buckling was formed because of the mechanical property mismatch between the active layer and PDMS. By measuring the wavelength of the buckling formed on the thin films, the Young's modulus of the thin films could be calculated by the following equation (6)

$$E_f = 3E_s \left(\frac{1 - \nu_f^2}{1 - \nu_s^2} \right) \left(\frac{\lambda}{2\pi d_f} \right)^3$$

where E_f , E_s , ν_f , ν_s , λ , and d_f are the Young's moduli of the thin film and substrate, Poisson's ratios of the thin film and substrate, wavelength of the buckling, and thickness of the thin film, respectively (46–48).

T_g of *is*-EMLs was analyzed by DMA. DMA was conducted following the ASTM D4065 standard. The size of the specimens was 40 mm long, 6 mm wide, and 50 μm thick. The temperature range was –50° to 100°C with a temperature increase rate of 2°C min⁻¹. The oscillation strain was 0.1% with a frequency of 1 Hz. T_g of pristine SY and *is*-EMLs was located at the peak position of the loss tangent.

Electrical characterization of *is*-EMLs and *is*-HTL

To characterize *is*-EMLs, hole- and electron-only devices were fabricated as schematically described and shown in figs. S3 and S4, respectively. For the hole-only device, ITO with a thickness of 100 nm was deposited on a glass substrate using a DC magnetron sputtering system. Then, pristine HTL was spin-coated on the ITO-deposited glass at 4000 rpm for 60 s and annealed at 120°C for 10 min. After that, the samples were transferred to a N₂-filled glove box. On top of HTL, pristine SY or an *is*-EML was spin-coated at 1500 rpm for 30 s. Then, the samples were thermally annealed at 90°C for 5 min. After annealing, the samples were transferred to a thermal evaporation chamber to deposit 100-nm-thick Au.

For the electron-only device, Ag with a thickness of 80 nm was deposited on the glass substrate using the thermal evaporator. d-PEIE was then used to modify the Ag cathode (38). For the d-PEIE solution, 0.25 wt % of PEIE (Sigma-Aldrich) and Cs₂CO₃ (Sigma-Aldrich) were co-dissolved in 2-ethoxyethanol (the weight ratio of PEIE to Cs₂CO₃ was 10:1). d-PEIE was spin-coated at 5000 rpm for 30 s and annealed at 100°C for 5 min. Then, the samples were transferred to the N₂ gas–filled glove box. On top of d-PEIE/Ag, pristine SY or *is*-EML was spin-coated at 1500 rpm for 30 s and thermally annealed at 90°C for 5 min. After that, d-PEIE was spin-coated on EML at 5000 rpm for 30 s, followed by thermal annealing at 90°C for 5 min. Last, the samples were transferred to the thermal evaporation chamber to deposit 100-nm-thick Al cathodes.

The current density (J) and voltage (V) of the hole-only devices were measured using a Keithley 2400 source meter. μ_h and μ_e of the materials for EML were calculated on the basis of the space charge-limited current (SCLC) model. In the SCLC model, μ can be calculated by the Mott-Gurney equation (16)

$$J = \frac{9\epsilon_r\epsilon_0\mu V^2}{8d^3}$$

where ϵ_r is the relative dielectric constant of the EML material, ϵ_0 is the permittivity of free space, d is the thickness of EML, and V is the effective applied voltage in the device ($V = V_{\text{applied}} - V_{\text{bi}} - V_r$, where V_{applied} is the applied voltage, V_{bi} is the built-in voltage, which is the relative work function difference between the anode and cathode, and V_r is the voltage applied by the series and contact resistance potential drop).

OLEDs and HTL-only devices were fabricated to analyze the hole transport properties of *is*-HTL. The schematic structures of the HTL-only device and conventional OLED are shown in fig. S8, A and B, respectively. For the HTL-only device, 100-nm-thick ITO was deposited on a glass substrate using the DC magnetron sputter. Pristine HTL or *is*-HTL was then spin-coated on ITO at 1000 rpm for 60 s and annealed at 120°C for 10 min. Last, 100-nm-thick Au was deposited using the thermal evaporation system. For the conventional OLEDs, ITO with a thickness of 100 nm was deposited on a glass substrate using the DC magnetron sputter. Then, pristine HTL or *is*-HTL was spin-coated on ITO at 4000 rpm for 60 s. Then, the samples were thermally annealed at 120°C for 10 min. After that, the samples were transferred to the N₂-filled glove box. For EML, pristine SY was spin-coated at 1500 rpm for 30 s and annealed at 90°C for 5 min. For ETL, d-PEIE was spin-coated at 5000 rpm for 30 s and annealed at 100°C for 5 min. After that, the samples were transferred to the thermal evaporation chamber to deposit a 100-nm-thick Al cathode. J , V , and L (luminance) of OLEDs were measured using a source meter and a Konica Minolta Cs-200 chromameter.

Other characterization methods of *is*-EMLs and *is*-HTL

For UV-vis absorption analysis, pristine SY and *is*-EMLs were spin-coated on glass substrates at 1500 rpm for 30 s in the N₂-filled glove box. For Raman spectroscopy analysis of EML, pristine SY and *is*-EMLs were spin-coated on Si wafer substrates at 1500 rpm for 30 s in the N₂-filled glove box. In addition, Triton X dissolved in toluene at a concentration of 5 mg ml⁻¹ was also spin-coated on a Si wafer as a reference. The wavelength of the laser was 785 nm with an exposure time of 100 s.

For Raman spectroscopy analysis of HTL, pristine HTL and *is*-HTL were spin-coated on glass substrates at 1000 rpm for 60 s. The wavelength of the laser was 532 nm with an exposure time of 60 s. For XPS analysis, pristine HTL and *is*-HTL were spin-coated on a Si wafer. XPS analysis was performed using a monochromated Al K α x-ray source. For microstructural analysis, tapping mode AFM (Park Systems) was used.

For the solvent orthogonality tests, solvents used in the fabrication of *is*-OLEDs were spin-coated on the surface of EML or HTL. For EML, pure isopropyl alcohol or 2-methoxyethanol was spin-coated on the EML-coated glass and annealed at 90°C for 5 min. For HTL, pure toluene was spin-coated on the HTL-coated glass and annealed at 90°C for 5 min. UV-vis absorption, OM, and Raman spectroscopy analysis were then used to determine the variations in the functional layers.

Preparation and characterization methods of *is*-ETL and *is*-cathode

For *is*-ETL, a ZnO nanoparticle dispersion and a d-PEIE solution were prepared. ZnO nanoparticles with a diameter of 110 nm (Sigma-Aldrich) were diluted to 3 wt % using isopropyl alcohol. The ZnO nanoparticle solution was sonicated using an ultrasonication bath before use. For the d-PEIE solution, 3 wt % PEIE (Sigma-Aldrich)

and Cs₂CO₃ (Sigma-Aldrich) were co-dissolved in 2-methoxyethanol (the weight ratio of PEIE to Cs₂CO₃ was 10:1). The d-PEIE solution was stirred at 80°C for 6 hours.

For microstructural characterization, ZnO dispersion and d-PEIE solution were spin-coated on AgNW network-embedded PDMS. The detailed preparation process for the AgNW-embedded PDMS is described below (38). Before spin coating, the AgNW-embedded PDMS was O₂ plasma-treated at 140 W for 90 s. ZnO dispersion was spin-coated at 1000 rpm for 30 s and annealed at 90°C for 5 min. On the ZnO nanoparticles, d-PEIE was spin-coated at 5000 rpm for 30 s and annealed at 90°C for 5 min. These processes were performed under ambient air conditions. The microstructure of *is*-ETL was analyzed using FE-SEM.

For electrical characterization, OLEDs with a discrete layer of *is*-ETL and OLEDs with a composite structure were fabricated. A schematic structure of each OLED is shown in fig. S10B. For OLEDs, ITO, *is*-HTL, and pristine SY were formed on a glass substrate as previously mentioned. On top of pristine SY, ZnO dispersion was spin-coated at 1000 rpm for 30 s in the N₂-filled glove box and annealed at 90°C for 5 min. The d-PEIE solution was spin-coated at 5000 rpm for 30 s in the N₂-filled glove box and annealed at 90°C for 5 min. After annealing d-PEIE, the samples were transferred to ambient atmosphere. Masking tape (Kapton tape) was used to define the cathode area. The AgNW solution (with a diameter of 30 nm and a length of 30 μ m; Novarials) at a concentration of 2.5 mg ml⁻¹ was spin-coated two times at 500 rpm for 30 s to form the cathode. AgNWs were annealed at 90°C for 5 min. For the composite structure, *is*-ETL was coated on AgNWs following the same process mentioned above.

Static and cyclic stretching tests were performed on *is*-cathode with composite structure. PDMS films were prepared by mixing the base and curing agent (Sylgard 184 elastomer kit from Dow Corning) at a weight ratio of 10:1. This liquid mixture was spin-coated at 500 rpm for 30 s on a PET substrate and cured at 120°C for 12 hours. The cured PDMS films were then peeled off from the PET substrate. On the PDMS films, ZnO nanoparticles were spin-coated at 1000 rpm for 30 s and annealed at 90°C for 5 min. Before spin coating ZnO nanoparticles, the surface of PDMS was O₂ plasma-treated at 140 W for 90 s. On ZnO, d-PEIE was spin-coated at 5000 rpm for 30 s and annealed at 90°C for 5 min. A AgNW dispersion with a concentration of 2.5 mg ml⁻¹ was then spin-coated three times at 500 rpm for 30 s and annealed at 90°C for 5 min. On the AgNW cathode, ZnO nanoparticles were spin-coated at 500 rpm for 30 s and annealed at 90°C for 5 min. Last, the d-PEIE solution was coated at 1000 rpm for 30 s, followed by annealing at 90°C for 10 min.

For static stretching tests, the strain was applied from 0 to 100% with a stretching rate of 10% s⁻¹, and electrical resistance (R) was measured using a digital multimeter (DMM). The cyclic stretching test was performed at 20 and 40% strain at a stretching rate of 20 and 40% s⁻¹, respectively. The change in R was measured using DMM. After stretching tests, the surface of the composite structured cathode was analyzed using FE-SEM.

Fabrication of *is*-OLEDs and characterization methods

Schematic descriptions for the fabrication processes of *is*-OLEDs were shown in fig. S12. For *is*-anode, AgNWs and aerogel nanoparticles (JIOS Aerogel) were co-embedded in a PDMS matrix. A AgNW concentration of 5 mg ml⁻¹ was spin-coated two times on a PET substrate at 500 rpm for 30 s and annealed at 100°C for 5 min. The

anode area was defined using a cotton swab. On AgNWs, an aerogel dispersion with 4 wt % ethanol was spin-coated at 1000 rpm for 30 s, followed by annealing at 100°C for 10 min. Then, a liquid mixture of PDMS was spin-coated at 300 rpm for 30 s, and PDMS was cured at 120°C for 12 hours. After curing PDMS, the AgNW-embedded PDMS was released from the PET substrate.

On *is*-anode, the *is*-HTL solution was spin-coated. Before coating *is*-HTL, *is*-anode was O₂ plasma-treated at 140 W for 90 s. *is*-HTL was spin-coated at 1000 rpm for 60 s and annealed at 90°C for 10 min. Then, the samples were transferred to the N₂-filled glove box. *is*-EML was spin-coated at 1500 rpm for 30 s, followed by annealing at 90°C for 5 min. For *is*-OLEDs with various colors, a red-orange light-emitting PPV-based copolymer (Sigma-Aldrich) dissolved in toluene at a concentration of 5 mg ml⁻¹ for the red *is*-OLED, a green light-emitting spiro-based copolymer (Sigma-Aldrich) dissolved in toluene at a concentration of 8 mg ml⁻¹ for the green *is*-OLED, and poly(9,9-di-*n*-octylfluorenyl-2,7-diyl) (Sigma-Aldrich) dissolved in toluene at a concentration of 5 mg ml⁻¹ for the blue *is*-OLED were used. ZnO nanoparticles were spin-coated at 1000 rpm for 30 s and annealed at 90°C for 5 min. On ZnO, d-PEIE was spin-coated at 5000 rpm for 30 s and annealed at 90°C for 5 min. After annealing d-PEIE, the samples were moved to ambient atmosphere, and the cathode area was defined using masking tape. Then, a AgNW dispersion with a concentration of 2.5 mg ml⁻¹ was spin-coated two times at 500 rpm for 30 s and annealed at 90°C for 5 min. On the AgNW cathode, ZnO nanoparticles were spin-coated at 500 rpm for 30 s and annealed at 90°C for 5 min. Last, the d-PEIE solution was coated at 1000 rpm for 30 s, followed by annealing at 90°C for 10 min. Then, the masking tape was removed, and the anode was exposed by removing the *is*-ETL layer.

J, *V*, and *L* of *is*-OLEDs were measured using a source meter and a chromameter. For electrical contact, liquid metal (InGa eutectic, Sigma-Aldrich) was applied on both the anode and cathode of *is*-OLEDs. For mechanical characterization, static and cyclic stretching tests were performed. For the static stretching test, *V* was applied during stretching up to 20, 40, 60, and 80% strain. The stretching rate was 80% s⁻¹. The cyclic stretching test was performed at 20, 40, and 50% strain with a stretching rate of 80% s⁻¹ for various stretching cycles.

is-OLEDs were analyzed using cross-sectional TEM analysis. For cross-sectional analysis, the surface of *is*-OLEDs was milled using focused ion beam to extract the cross section of *is*-OLEDs. The cross section of *is*-OLEDs was observed, and the atomic components were analyzed through EDS mapping. For lifetime analysis, *is*-OLEDs were operated at a voltage of 9.3 V, and *J*-*V*-*L* characteristics were regularly measured every 3 s.

SUPPLEMENTARY MATERIALS

Supplementary material for this article is available at <http://advances.sciencemag.org/cgi/content/full/7/9/eabd9715/DC1>

REFERENCES AND NOTES

- J. J. Liang, L. Li, X. F. Niu, Z. B. Yu, Q. B. Pei, Elastomeric polymer light-emitting devices and displays. *Nat. Photonics* **7**, 817–824 (2013).
- D.-H. Kim, N. Lu, R. Ma, Y.-S. Kim, R.-H. Kim, S. Wang, J. Wu, S. M. Won, H. Tao, A. Islam, K. J. Yu, T.-i. Kim, R. Chowdhury, M. Ying, L. Xu, M. Li, H.-J. Chung, H. Keum, M. McCormick, P. Liu, Y.-W. Zhang, F. G. Omenetto, Y. Huang, T. Coleman, J. A. Rogers, Epidermal electronics. *Science* **333**, 838–843 (2011).
- T. Yokota, P. Zalar, M. Kaltenbrunner, H. Jinno, N. Matsuhisa, H. Kitanosako, Y. Tachibana, W. Yukita, M. Koizumi, T. Someya, Ultraflexible organic photonic skin. *Sci. Adv.* **2**, e1501856 (2016).
- C. Larson, B. Peele, S. Li, S. Robinson, M. Totaro, L. Beccai, B. Mazzolai, R. Shepherd, Highly stretchable electroluminescent skin for optical signaling and tactile sensing. *Science* **351**, 1071–1074 (2016).
- T. Sekitani, H. Nakajima, H. Maeda, T. Fukushima, T. Aida, K. Hata, T. Someya, Stretchable active-matrix organic light-emitting diode display using printable elastic conductors. *Nat. Mater.* **8**, 494–499 (2009).
- J. Y. Oh, S. Rondeau-Gagné, Y. C. Chiu, A. Chortos, F. Lissel, G. J. N. Wang, B. C. Schroeder, T. Kurosawa, J. Lopez, T. Katsumata, J. Xu, C. X. Zhu, X. D. Gu, W. G. Bae, Y. Kim, L. H. Jin, J. W. Chung, J. B. H. Tok, Z. N. Bao, Intrinsically stretchable and healable semiconducting polymer for organic transistors. *Nature* **539**, 411–415 (2016).
- T. Sekitani, Y. Noguchi, K. Hata, T. Fukushima, T. Aida, T. Someya, A rubberlike stretchable active matrix using elastic conductors. *Science* **321**, 1468–1472 (2008).
- J. H. Hong, J. M. Shin, G. M. Kim, H. Joo, G. S. Park, I. B. Hwang, M. W. Kim, W. S. Park, H. Y. Chu, S. Kim, 9.1-inch stretchable AMOLED display based on LTPS technology. *J. Soc. Inf. Display* **25**, 194–199 (2017).
- R.-H. Kim, D.-H. Kim, J. Xiao, B. H. Kim, S.-I. Park, B. Panilaitis, R. Ghaffari, J. Yao, M. Li, Z. Liu, V. Malyarchuk, D. G. Kim, A.-P. Le, R. G. Nuzzo, D. L. Kaplan, F. G. Omenetto, Y. Huang, Z. Kang, J. A. Rogers, Waterproof AllnGaP optoelectronics on stretchable substrates with applications in biomedicine and robotics. *Nat. Mater.* **9**, 929–937 (2010).
- S. H. Wang, J. Xu, W. C. Wang, G. J. N. Wang, R. Rastak, F. Molina-Lopez, J. W. Chung, S. M. Niu, V. R. Feig, J. Lopez, T. Lei, S. K. Kwon, Y. Kim, A. M. Foudeh, A. Ehrlich, A. Gasperini, Y. Yun, B. Murmann, J. B. H. Tok, Z. A. Bao, Skin electronics from scalable fabrication of an intrinsically stretchable transistor array. *Nature* **555**, 83–88 (2018).
- J. Kim, G. A. Salvatore, H. Araki, A. M. Chiarelli, Z. Xie, A. Banks, X. Sheng, Y. Liu, J. W. Lee, K.-I. Jang, S. Y. Heo, K. Cho, H. Luo, B. Zimmerman, J. Kim, L. Yan, X. Feng, S. Xu, M. Fabiani, G. Gratton, Y. Huang, U. Paik, J. A. Rogers, Battery-free, stretchable optoelectronic systems for wireless optical characterization of the skin. *Sci. Adv.* **2**, e1600418 (2016).
- J. Xu, S. H. Wang, G. J. N. Wang, C. X. Zhu, S. C. Luo, L. H. Jin, X. D. Gu, S. C. Chen, V. R. Feig, J. W. F. To, S. Rondeau-Gagne, J. Park, B. C. Schroeder, C. Lu, J. Y. Oh, Y. M. Wang, Y. H. Kim, H. Yan, R. Sinclair, D. S. Zhou, G. Xue, B. Murmann, C. Linder, W. Cai, J. B. H. Tok, J. W. Chung, Z. N. Bao, Highly stretchable polymer semiconductor films through the nanoconfinement effect. *Science* **355**, 59–64 (2017).
- J. Liang, L. Li, K. Tong, Z. Ren, W. Hu, X. Niu, Y. Chen, Q. Pei, Silver nanowire percolation network soldered with graphene oxide at room temperature and its application for fully stretchable polymer light-emitting diodes. *ACS Nano* **8**, 1590–1600 (2014).
- Z. Yu, X. Niu, Z. Liu, Q. Pei, Intrinsically stretchable polymer light-emitting devices using carbon nanotube-polymer composite electrodes. *Adv. Mater.* **23**, 3989–3994 (2011).
- S. E. Root, S. Savagatrup, A. D. Printz, D. Rodriguez, D. J. Lipomi, Mechanical properties of organic semiconductors for stretchable, highly flexible, and mechanically robust electronics. *Chem. Rev.* **117**, 6467–6499 (2017).
- S. Chen, S. Jung, H. J. Cho, N.-H. Kim, S. Jung, J. Xu, J. Oh, Y. Cho, H. Kim, B. Lee, Y. An, C. Zhang, M. Xiao, H. Ki, Z.-G. Zhang, J.-Y. Kim, Y. Li, H. Park, C. Yang, Highly flexible and efficient all-polymer solar cells with high-viscosity processing polymer additive toward potential of stretchable devices. *Angew. Chem. Int. Ed.* **57**, 13277–13282 (2018).
- S. Gambino, A. K. Bansal, I. D. W. Samuel, Comparison of hole mobility in thick and thin films of a conjugated polymer. *Org. Electron.* **11**, 467–471 (2010).
- S. R. Tseng, Y. S. Chen, H. F. Meng, H. C. Lai, C. H. Yeh, S. F. Horng, H. H. Liao, C. S. Hsu, Electron transport and electroluminescent efficiency of conjugated polymers. *Synth. Met.* **159**, 137–141 (2009).
- Y. Zheng, G.-J. N. Wang, J. Kang, M. Nikolka, H.-C. Wu, H. Tran, S. Zhang, H. Yan, H. Chen, P. Y. Yuen, J. Mun, R. H. Dauskardt, I. McCulloch, J. B. H. Tok, X. Gu, Z. Bao, An intrinsically stretchable high-performance polymer semiconductor with low crystallinity. *Adv. Funct. Mater.* **29**, 1905340 (2019).
- G. J. N. Wang, A. Gasperini, Z. A. Bao, Stretchable polymer semiconductors for plastic electronics. *Adv. Electron. Mater.* **4**, 1700429 (2018).
- S. Burns, J. MacLeod, T. Trang Do, P. Sonar, S. D. Yambem, Effect of thermal annealing Super Yellow emissive layer on efficiency of OLEDs. *Sci. Rep.* **7**, 40805 (2017).
- T.-Q. Nguyen, I. B. Martini, J. Liu, B. J. Schwartz, Controlling interchain interactions in conjugated polymers: The effects of chain morphology on exciton–exciton annihilation and aggregation in MEH–PPV films. *J. Phys. Chem. B* **104**, 237–255 (2000).
- E. Mulazzi, A. Ripamonti, J. Wery, B. Dulieu, S. Lefrant, Theoretical and experimental investigation of absorption and Raman spectra of poly(paraphenylene vinylene). *Phys. Rev. B* **60**, 16519–16525 (1999).
- L. Feng, F. Wang, M.-S. Niu, F. Zheng, P.-Q. Bi, X.-Y. Yang, W.-L. Xu, X.-T. Hao, Structural and optical properties of conjugated polymer and carbon-based non-fullerene material blend films for photovoltaic applications. *Opt. Mater. Express* **7**, 687–697 (2017).
- R. Traiphop, P. Sanguansat, T. Srihirin, T. Kerdcharoen, T. Osotchan, Spectroscopic study of photophysical change in collapsed coils of conjugated polymers: Effects of solvent and temperature. *Macromolecules* **39**, 1165–1172 (2006).
- J. Kim, T. M. Swager, Control of conformational and interpolymer effects in conjugated polymers. *Nature* **411**, 1030–1034 (2001).

27. V. V. Bruevich, T. S. Makhmutov, S. G. Elizarov, E. M. Nechvolodova, D. Y. Paraschuk, Raman spectroscopy of intermolecular charge transfer complex between a conjugated polymer and an organic acceptor molecule. *J. Chem. Phys.* **127**, 104905 (2007).
28. P. Prins, F. C. Grozema, L. D. A. Siebbeles, Efficient charge transport along phenylene–vinylene molecular wires. *J. Phys. Chem. B* **110**, 14659–14666 (2006).
29. S. Prodhon, J. Qiu, M. Ricci, O. M. Rosconi, L. Wang, D. Beljonne, Design rules to maximize charge-carrier mobility along conjugated polymer chains. *J. Phys. Chem. Lett.* **11**, 6519–6525 (2020).
30. J. Y. Oh, S. Kim, H.-K. Baik, U. Jeong, Conducting polymer dough for deformable electronics. *Adv. Mater.* **28**, 4455–4461 (2016).
31. M. Y. Teo, N. Kim, S. Kee, B. S. Kim, G. Kim, S. Hong, S. Jung, K. Lee, Highly stretchable and highly conductive PEDOT:PSS/ionic liquid composite transparent electrodes for solution-processed stretchable electronics. *ACS Appl. Mater. Interfaces* **9**, 819–826 (2017).
32. Y. Wang, C. Zhu, R. Pfattner, H. Yan, L. Jin, S. Chen, F. Molina-Lopez, F. Lissel, J. Liu, N. I. Rabiah, Z. Chen, J. W. Chung, C. Linder, M. F. Toney, B. Murmann, Z. Bao, A highly stretchable, transparent, and conductive polymer. *Sci. Adv.* **3**, e1602076 (2017).
33. B. Xu, S.-A. Gopalan, A.-I. Gopalan, N. Muthuchamy, K.-P. Lee, J.-S. Lee, Y. Jiang, S.-W. Lee, S.-W. Kim, J.-S. Kim, H.-M. Jeong, J.-B. Kwon, J.-H. Bae, S.-W. Kang, Functional solid additive modified PEDOT:PSS as an anode buffer layer for enhanced photovoltaic performance and stability in polymer solar cells. *Sci. Rep.* **7**, 45079 (2017).
34. H. Zheng, Y. Zheng, N. Liu, N. Ai, Q. Wang, S. Wu, J. Zhou, D. Hu, S. Yu, S. Han, W. Xu, C. Luo, Y. Meng, Z. Jiang, Y. Chen, D. Li, F. Huang, J. Wang, J. Peng, Y. Cao, All-solution processed polymer light-emitting diode displays. *Nat. Commun.* **4**, 1971 (2013).
35. A. Armin, R. D. Jansen-van Vuuren, N. Kopidakis, P. L. Burn, P. Meredith, Narrowband light detection via internal quantum efficiency manipulation of organic photodiodes. *Nat. Commun.* **6**, 6343 (2015).
36. J. Ouyang, Q. Xu, C.-W. Chu, Y. Yang, G. Li, J. Shinar, On the mechanism of conductivity enhancement in poly(3,4-ethylenedioxythiophene):poly(styrene sulfonate) film through solvent treatment. *Polymer* **45**, 8443–8450 (2004).
37. Y. Zhou, C. Fuentes-Hernandez, J. Shim, J. Meyer, A. J. Giordano, H. Li, P. Winget, T. Papadopoulos, H. Cheun, J. Kim, M. Fenoll, A. Dindar, W. Haske, E. Najafabadi, T. M. Khan, H. Sojoudi, S. Barlow, S. Graham, J.-L. Brédas, S. R. Marder, A. Kahn, B. Kippelen, A universal method to produce low-work function electrodes for organic electronics. *Science* **336**, 327–332 (2012).
38. J.-H. Kim, J.-W. Park, Designing an electron-transport layer for highly efficient, reliable, and solution-processed organic light-emitting diodes. *J. Mater. Chem. C* **5**, 3097–3106 (2017).
39. S. L. Clark, P. T. Hammond, The role of secondary interactions in selective electrostatic multilayer deposition. *Langmuir* **16**, 10206–10214 (2000).
40. S. Ohisa, T. Kato, T. Takahashi, M. Suzuki, Y. Hayashi, T. Koganezawa, C. R. McNeill, T. Chiba, Y.-J. Pu, J. Kido, Conjugated polyelectrolyte blend with polyethyleneimine ethoxylated for thickness-insensitive electron injection layers in organic light-emitting devices. *ACS Appl. Mater. Interfaces* **10**, 17318–17326 (2018).
41. X. Dai, Z. Zhang, Y. Jin, Y. Niu, H. Cao, X. Liang, L. Chen, J. Wang, X. Peng, Solution-processed, high-performance light-emitting diodes based on quantum dots. *Nature* **515**, 96–99 (2014).
42. J. Kim, J. Park, U. Jeong, J.-W. Park, Silver nanowire network embedded in polydimethylsiloxane as stretchable, transparent, and conductive substrates. *J. Appl. Polym. Sci.* **133**, 43830 (2016).
43. S. G. R. Bade, X. Shan, P. T. Hoang, J. Li, T. Geske, L. Cai, Q. Pei, C. Wang, Z. Yu, Stretchable light-emitting diodes with organometal-halide-perovskite-polymer composite emitters. *Adv. Mater.* **29**, 1607053 (2017).
44. W. H. Koo, S. M. Jeong, F. Araoka, K. Ishikawa, S. Nishimura, T. Toyooka, H. Takezoe, Light extraction from organic light-emitting diodes enhanced by spontaneously formed buckles. *Nat. Photonics* **4**, 222–226 (2010).
45. T.-H. Han, M.-R. Choi, C.-W. Jeon, Y.-H. Kim, S.-K. Kwon, T.-W. Lee, Ultrahigh-efficiency solution-processed simplified small-molecule organic light-emitting diodes using universal host materials. *Sci. Adv.* **2**, e1601428 (2016).
46. J.-H. Kim, S.-R. Kim, H.-J. Kil, Y.-C. Kim, J.-W. Park, Highly conformable, transparent electrodes for epidermal electronics. *Nano Lett.* **18**, 4531–4540 (2018).
47. J. Du, V. C. Anye, E. O. Vodah, T. Tong, M. G. Zebaze Kana, W. O. Soboyejo, Pressure-assisted fabrication of organic light emitting diodes with MoO₃ hole-injection layer materials. *J. Appl. Phys.* **115**, 233703 (2014).
48. S. Dogru, B. Aksoy, H. Bayraktar, B. E. Alaca, Poisson's ratio of PDMS thin films. *Polym. Test* **69**, 375–384 (2018).

Acknowledgments

Funding: J.-H.K. and J.-W.P. acknowledge the support from the National Research Foundation of Korea (NRF), the Ministry of Science, ICT and Future Planning (grant number 2018R1A2B6001390). This research was also supported by the Graduate School of Yonsei University Research Scholarship Grants in 2019. **Author contributions:** J.-H.K. and J.-W.P. designed the project. J.-H.K. carried out the experiments and analysis. J.-H.K. and J.-W.P. wrote the paper. **Competing interests:** The authors declare that they have no competing interests. **Data and materials availability:** All data needed to evaluate the conclusions in the paper are present in the paper and/or the Supplementary Materials. Additional data related to this paper may be requested from the authors.

Submitted 23 July 2020

Accepted 8 January 2021

Published 24 February 2021

10.1126/sciadv.abd9715

Citation: J.-H. Kim, J.-W. Park, Intrinsically stretchable organic light-emitting diodes. *Sci. Adv.* **7**, eabd9715 (2021).

Intrinsically stretchable organic light-emitting diodes

Jin-Hoon Kim and Jin-Woo Park

Sci Adv 7 (9), eabd9715.

DOI: 10.1126/sciadv.abd9715

ARTICLE TOOLS

<http://advances.sciencemag.org/content/7/9/eabd9715>

SUPPLEMENTARY MATERIALS

<http://advances.sciencemag.org/content/suppl/2021/02/22/7.9.eabd9715.DC1>

REFERENCES

This article cites 48 articles, 9 of which you can access for free
<http://advances.sciencemag.org/content/7/9/eabd9715#BIBL>

PERMISSIONS

<http://www.sciencemag.org/help/reprints-and-permissions>

Use of this article is subject to the [Terms of Service](#)

Science Advances (ISSN 2375-2548) is published by the American Association for the Advancement of Science, 1200 New York Avenue NW, Washington, DC 20005. The title *Science Advances* is a registered trademark of AAAS.

Copyright © 2021 The Authors, some rights reserved; exclusive licensee American Association for the Advancement of Science. No claim to original U.S. Government Works. Distributed under a Creative Commons Attribution NonCommercial License 4.0 (CC BY-NC).